Electronically- and crystal-structure-driven magnetic structures and physical properties of RScSb (R = rare earth) compounds: a neutron diffraction, magnetization and heat capacity study

2014 J. Phys.: Condens. Matter 26 366001

(http://iopscience.iop.org/0953-8984/26/36/366001)

IOP Publishing
Journal of Physics: Condensed Matter
J. Phys.: Condens. Matter **26** (2014) 366001 (13pp)
doi:10.1088/0953-8984/26/36/366001

Electronically- and crystal-structure-driven magnetic structures and physical properties of RScSb (R = rare earth) compounds: a neutron diffraction, magnetization and heat capacity study

C Ritter[1], S K Dhar[2], R Kulkarni[2], A Provino[3,4,5], D Paudyal[5], P Manfrinetti[3,4,5] and K A Gschneidner[5,6]

[1] Institut Laue-Langevin, BP 156, 38042 Grenoble, France
[2] Department of Condensed Matter Physics & Material Science, T.I.F.R., Homi Bhabha Road, Mumbai 400005, India
[3] Institute SPIN-CNR, Corso Perrone 24, 16152 Genova, Italy
[4] Department of Chemistry, University of Genova, Via Dodecaneso 31, 16146 Genova, Italy
[5] The Ames Laboratory, U.S. Department of Energy, Iowa State University, Ames, IA 50011–3020, USA
[6] Department of Materials Science and Engineering, Iowa State University, Ames, IA 50011–2300, USA

E-mail: ritter@ill.fr

Received 16 May 2014, revised 11 June 2014
Accepted for publication 21 July 2014
Published 14 August 2014

Abstract

The synthesis of the new equiatomic RScSb (R = La-Nd, Sm, Gd-Tm, Lu, Y) compounds has been recently reported. These rare earth compounds crystallize in two different crystal structures, adopting the CeScSi-type ($I4/mmm$) for the lighter R (La-Nd, Sm) and the CeFeSi-type ($P4/nmm$) structure for the heavier R (R = Gd-Tm, Lu, Y). Here we report the results of neutron diffraction, magnetization and heat capacity measurements on some of these compounds (R = Ce, Pr, Nd, Gd and Tb). Band structure calculations have also been performed on CeScSb and GdScGe (CeScSi-type), and on GdScSb and TbScSb (CeFeSi-type) to compare and understand the exchange interactions in CeScSi and CeFeSi structure types. The neutron diffraction investigation shows that all five compounds order magnetically, with the highest transition temperature of 66 K in TbScSb and the lowest of about 9 K in CeScSb. The magnetic ground state is simple ferromagnetic ($\tau = [0\ 0\ 0]$) in CeScSb, as well in NdScSb for $32 > T > 22$ K. Below 22 K a second magnetic transition, with propagation vector $\tau = [¼\ ¼\ 0]$, appears in NdScSb. PrScSb has a magnetic structure within, determined by mostly ferromagnetic interactions and antiferromagnetic alignment of the Pr-sites connected through the I-centering ($\tau = [1\ 0\ 0]$). A cycloidal spiral structure with a temperature dependent propagation vector $\tau = [\delta\ \delta\ ½]$ is found in TbScSb. The results of magnetization and heat capacity lend support to the main conclusions derived from neutron diffraction. As inferred from a sharp peak in magnetization, GdScSb orders antiferromagnetically at 56 K. First principles calculations show lateral shift of spin split bands towards lower energy from the Fermi level as the CeScSi-type structure changes to the CeFeSi-type structure. This rigid shift may force the system to transform from exchange split ferromagnetic state to the antiferromagnetic state in RScSb compounds (as seen for example in GdScSb and TbScSb) and is proposed to explain the change-over from a ferromagnetic structure as found in the CeScSi-type compounds CeScSb and NdScSb to the antiferromagnetic state as found in TbScSb and GdScSb.

Keywords: rare earth ternary compounds, rare earth scandium antimonides, magnetic properties, magnetic structures, neutron diffraction

(Some figures may appear in colour only in the online journal)

1. Introduction

The ternary equiatomic compounds RTX (where R = rare earth, T = transition metal, X = p-block element) are the most common phases formed in the R-T-X intermetallic systems [1, 2] and are among the most extensively investigated for the search of new magnetic materials [3]. In particular, the RScX and RTiX compounds with X = Si, Ge, and RZrSb crystallizing with the CeScSi-type structure, have been found to order ferromagnetically and characterized by high Curie temperatures and large coercive fields. In some cases the Curie temperature is comparable or even higher than that of Gd metal (T_C = 293 K [4]); e.g. T_C = 270 K for both SmScSi and SmScGe [5], T_C = 318 and 350 K for GdScSi and GdScGe, respectively [5, 6], T_C = 376 K for GdTiGe [7]. The magnetic structures of some RScGe (R = Pr, Nd, Tb [8, 9]), RTiGe (Pr, Nd, Tb-Er [10]), RMgSn [11, 12], and RZrSb (R = Tb, Ho, Er [13]) in their magnetically ordered state(s), have been recently studied by neutron diffraction.

In continuation of our focus on R-T-X systems, we have recently reported on the synthesis and crystal structure of a new family of equiatomic rare earth compounds RScSb [14]. Depending upon R, these compounds have been found to crystallize in two different crystal structures: compounds with light R (La-Nd, Sm) adopt the CeScSi-type structure (tetragonal *tI*12, *I*4/*mmm*, an ordered variant of the La_2Sb-type), while those with heavier R (R = Gd-Tm, Lu, Y) crystallize with the CeFeSi-type structure (tetragonal *tP*6, *P*4/*nmm*, an ordered derivative of the Cu_2Sb-type). Refinement of single crystal data for CeScSb and NdScSb led to satisfactory results only after the position of Sc atom was slightly moved from the 4*c* (0, ½, 0) to the 8*j* position (x, ½, 0), with an x value of about 0.075 and an occupational factor of 0.5 [14]. Eu and Yb do not form the equiatomic 1:1:1 phases, this being likely due to the divalent character of these two ions. First principles electronic structure calculations performed for some representative compounds showed that the differences in the crystal structure directly reflect into the differences in the electronic structures.

In the present work we have investigated the magnetic structure of the RScSb compounds for R = Ce, Pr, Nd and Tb by neutron diffraction, supplemented by the study of the magnetization as a function of temperature and field and by heat capacity data. Owing to the high neutron capture cross section for Gd ions no neutron diffraction was carried out for GdScSb, however, its magnetic behavior was probed by magnetization. First principles electronic structure calculations show that the different magnetic structures in the RScSb series are due to the differences in the crystal structures as well as in the hybridizations of the conduction electron states.

2. Experimental details

The samples were prepared by arc melting the elements under a pure argon atmosphere. The rare earth metals and antimony used to prepare the alloys were commercial products; stated purities were 99.9 wt.% for the rare earths (with respect to the other rare earths only, interstitial impurities and non-rare earth metals concentrations were not given) and 99.999 wt.% for Sb. Because of the volatility of elemental Sb, a 1.5 wt.% excess of Sb was added to compensate the average weight loss observed during the melting of alloys (2.0 wt.% excess Sb for Tb sample). The light R metals (Ce, Pr, Nd) were weighed and handled in a glove box under an inert atmosphere. The total mass of each sample was ≈7–8 g. The buttons were melted three times, turning them upside down each time. They were then wrapped in a Ta foil, sealed under vacuum in quartz ampoules and annealed at 900–1000 °C for 1–2 weeks; then slowly cooled down to room temperature. The resulting alloys have a dark-grey color and a metallic luster; they are crystalline, brittle, and moisture sensitive.

The samples were examined by x-ray powder diffraction, using a Guinier-Stoe camera (Cu Kα1 radiation, Si as internal standard, a = 5.4308(1) Å). The neutron diffraction data were taken on the high resolution powder diffractometer D1A and on the high intensity diffractometers D1B and partially D20, all situated at the Institut Laue Langevin at Grenoble, France. The thermal dependence of the neutron spectra (thermodiffractogram) was determined on D1B with λ = 2.52 Å for R = Nd and Tb, between 2 K and 38 K (R = Nd) and 2 K and 76 K (R = Tb), recording the spectra for 5 min every 1 K. PrScSb was measured at selected temperatures of 1.5 K, 10 K, 20 K, 30 K and 100 K on D1B for 25 min at each temperature, CeScSb for 2 h each at temperatures of 1.5 K, 10 K and 20 K. An additional thermodiffractogram of CeScSb was measured on D20 with λ = 2.4 Å between 1.7 K and 25 K recording spectra for 25 min every 1 K. High resolution data were taken on D1A with λ = 1.908 Å for all compounds at room temperature, and for R = Pr at 1.5 K and 40 K, R = Nd at 1.5 K, 25 K, 40 K, and R = Tb at 1.5 K, 40 K, 52 K, 62 K and 75 K between 0° < 2θ < 158° with a step-width of 0.1°. All neutron data were analyzed using the Rietveld refinement program FULLPROF [15]; sketches of the crystallographic and magnetic structures were drawn with the program Fullprof Studio [16] incorporated in [15].

Magnetization as a function of temperature and field was measured in a SQUID magnetometer (Quantum Design, USA), and the heat capacity was measured using the relaxation technique in a PPMS (Quantum Design, USA).

Table 1. Results of the Rietveld refinement of the high resolution neutron diffraction data at 300 K for RScSb compounds with CeScSi or CeFeSi structure type.

CeScSi-type (*I*4/*mmm*)	Ce	Pr	Nd
x_{Sc} (8*j*)	0.0752(6)	0.0429(9)	0.0568(7)
occ_{Sc}	0.440(4)	0.474(8)	0.450(2)
z_{Sb}(4*e*)	0.1256(2)	0.1260(2)	0.1273(2)
a [Å]	4.4540(2)	4.4360(1)	4.4149(2)
c [Å]	16.5098(9)	16.4184(6)	16.3806(7)
R_{Bragg}	4.8	6.9	6.5
CeFeSi-type (*P*4/*nmm*)	Tb		
z_{Tb}(2*c*)	0.6535(4)		
z_{Sb}(2*c*)	0.2934(6)		
a [Å]	4.3125(1)		
c [Å]	8.1353(3)		
R_{Bragg}	2.3		

3. Results and discussion

3.1. Room temperature high resolution neutron diffraction

The high resolution data recorded for the four RScSb compounds at room temperature were refined in order to verify the space group, to determine the atomic coordinates and to check for the presence of any impurity phases. While the refinement proceeded smoothly for NdScSb in *I*4/*mmm*, small amounts of impurity phases were found for the other three RScSb compounds. LeBail refinement of the impurity phase for *R* = Ce showed that the impurity peaks fulfilled the extinction conditions of the orthorhombic space group *Cmca* with lattice constants *a* = 6.3 Å, *b* = 6.1 Å and *c* = 18.21 Å, corresponding to the known phase of $CeSb_2$ [17] with the $LaSb_2$ type structure. A cubic phase with extinction conditions corresponding to the space group $Fm-3m$ with *a* = 6.3 Å was found for the Pr-compound pointing to the presence of PrSb [18] as impurity phase. $Tb_3Sc_2Sb_3$ [14] with *a* = 11.61 Å, *b* = 9.00 Å and *c* = 7.82 Å was identified as the impurity phase in TbScSb. These impurity phases were included as secondary phases in the Rietveld refinements of the three RScSb compounds (*R* = Ce, Pr, Tb), using the LeBail pattern matching mode.

As already found by a previous x-ray study, the compounds containing light rare earth atoms (*R* = Ce, Pr, Nd) crystallize in the CeScSi structure type with space group *I*4/*mmm*, while TbScSb adopts the CeFeSi-type structure (*P*4/*nmm*). In order to achieve a good refinement of the high resolution neutron diffraction data, a shift of the Sc atom position from the Wyckoff site 4*c* (0, ½, 0) towards the site 8*j* (*x*, ½, 0) together with a significant reduction of the occupation had to be allowed for all three CeScSi-type compounds, resulting in final stoichiometries of $CeSc_{0.88}Sb$, $PrSc_{0.95}Sb$ and $NdSc_{0.90}Sb$. Table 1 contains the results of the refinements of the room temperature data of the four RScSb compounds; figure 1 shows a plot of the refinement of the neutron diffraction data of PrScSb.

3.2. Low temperature neutron diffraction

3.2.1. NdScSb. Figure 2 displays the low angle region of the thermodiffractogram of NdScSb measured between 2 and 38 K. Two separate magnetic transitions can be discerned, the first one leads to an increase of intensity at 2θ positions corresponding to allowed nuclear Bragg peaks, whereas the second transition gives rise to new Bragg peaks appearing at 2θ positions not allowed by the symmetry of the nuclear unit cell. The integration of the intensity of the reflections furnishes the two transition temperatures of T_{C1} = 32 K and T_{C2} = 22 K (labeled as 1 and 2, respectively in figure 2). From the position of these magnetic Bragg peaks the magnetic propagation vectors were determined using the program K-Search, which is part of the FULLPROF suite of programs, to be τ_1 = [0 0 0] and τ_2 = [¼ ¼ 0].

Magnetic symmetry analysis using the program BASIREPS [19, 20] gave the allowed irreducible representations (IR) and their basis-vectors (BV) for the Nd position on the Wyckoff site 4*e* in space group *I*4/*mmm* as listed in table 2 for the two magnetic propagation vectors. For the magnetic phase appearing below T_{C1} = 32 K only IR's having ferromagnetic BV's have to be considered for the refinement of the magnetic structure. Therefore IR7 with a ferromagnetic BV in *c*-direction and IR10 with ferromagnetic BV's within the tetragonal *a*-*b* plane were considered using the high resolution data taken just above T_{C2} at 25 K. Only a magnetic structure where the magnetic moments are pointing in the *c*-direction is able to refine the data, the magnetic moment value amounting to 1.1(1)μ_B at *T* = 25 K. Therefore below T_{C1} = 32 K, NdScSb adopts first a simple ferromagnetic structure with moments pointing along the *c*-direction. The additional modulation of the magnetic moments resulting from the appearance of the second magnetic propagation vector τ_2 = [¼ ¼ 0] below T_{C2} = 22 K was modeled as a second magnetic phase in the refinement of the high resolution data taken at 1.5 K. Testing the four possible IR's only IR3 allowed a good refinement of the data. While the coefficient of BV2 refined to 1.65(6), the coefficient of BV1 did not adopt a significant value and was in the final refinement fixed to zero. At the same time the purely ferromagnetic component linked to τ_1 = [0 0 0] increased to 1.90 (5)μ_B at this temperature. We cannot exclude from our data the possibility that the two magnetic structures are present in spatially separated parts of the sample volume. If one, however, assumes that both magnetic structures embrace the whole sample volume, the maximum magnetic moment value on the Nd site amounts to 3.1(1)–3.5(1)μ_B depending on the phase between the two ordering schemes which cannot be determined from powder data. This value corresponds nicely to the maximum expected magnetic moment for the Nd^{3+} ion of 3.28μ_B. Figure 3 displays the magnetic structure resulting from the superposition of the two magnetic configurations assuming a phase shift of φ = ⅛ 2π.

3.2.2. TbScSb. The low angle part of the thermodiffractogram of TbScSb measured between *T* = 2 K and 76 K is shown in figure 4; it displays the appearance of new Bragg peaks at about *T* = 66 K. These new peaks are of magnetic origin and they change their 2θ position when lowering the temperature until *T* = 40 K. The peaks can be indexed with an incommensurate magnetic propagation vector τ = [δ δ ½] with δ increasing quickly from 0.21–0.239 as the temperature is reduced from 62–40 K. Below 40 K, the position of these incommensurate magnetic peaks changes only slightly on further cooling down to 2 K without reaching the commensurate

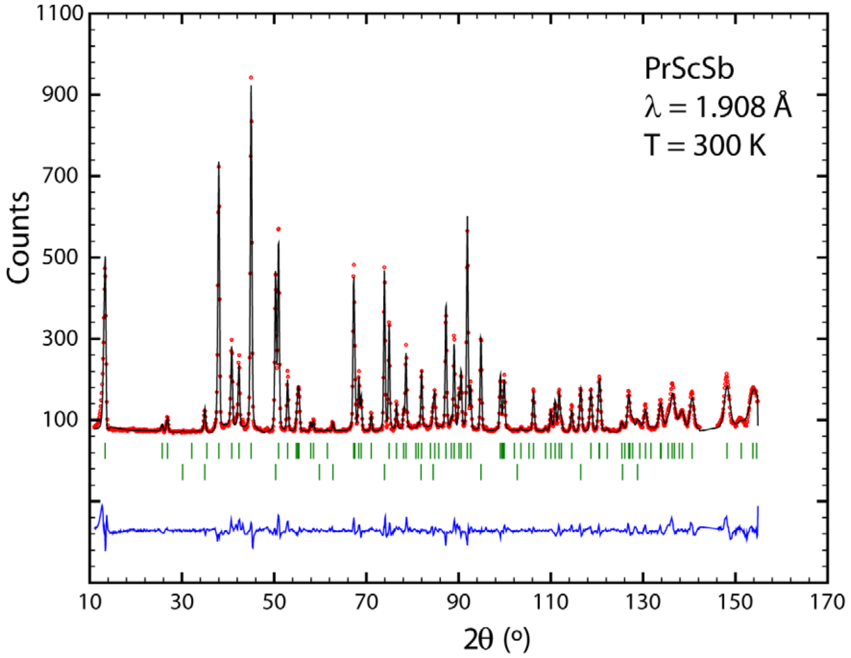

Figure 1. Observed (dots, red), calculated (line, black) and difference pattern of PrScSb at 300 K. The tick marks indicate the calculated position of the nuclear Bragg peaks of the main phase (upper row) and of the PrSb impurity phase (lower row).

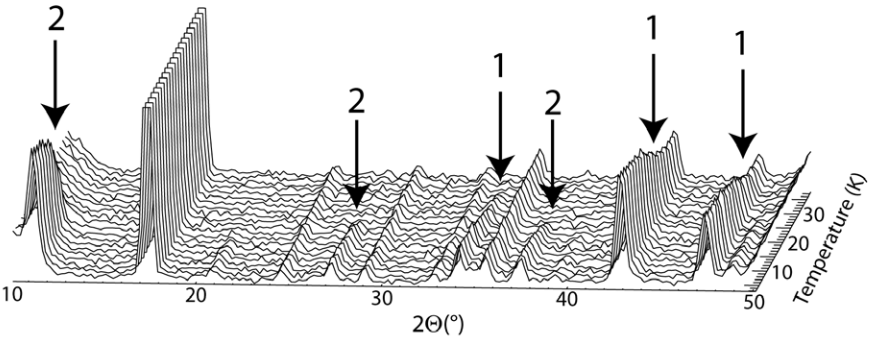

Figure 2. Thermal dependence of the neutron diffraction pattern of NdScSb between 2 K and 38 K.

Table 2. Basis-vectors (BV) of the allowed irreducible representations (IR) for $\tau_1 = [0\ 0\ 0]$ and $\tau_2 = [¼\ ¼\ 0]$ for the Wyckoff position 4*e* of space group *I*4/*mmm*.

$\tau = [0\ 0\ 0]$	BV1	BV2		BV1	BV2
IR2			IR9		
x, y, z	0 0 1		*x, y, z*	1 0 0	0 −1 0
−x, y, −z	0 0 −1		*−x, y, −z*	−1 0 0	0 1 0
IR7			IR10		
x, y, z	0 0 1		*x, y, z*	0 1 0	1 0 0
−x, y, −z	0 0 1		*−x, y, −z*	0 1 0	1 0 0
$\tau = [¼\ ¼\ 0]$	BV1	BV2		BV1	BV2
IR1			IR3		
x, y, z	1 −1 0		*x, y, z*	1 1 0	0 0 1
y, x, −z	−1 1 0		*y, x, −z*	−1 −1 0	0 0 1
IR2			IR4		
x, y, z	1 1 0	0 0 1	*x, y, z*	1 −1 0	
y, x, −z	1 1 0	0 0 −1	*y, x, −z*	1 −1 0	

value of 0.25. Additional new peaks appearing at about 35 K are not linked to the main compound TbScSb but originate in the impurity phase $Tb_3Sc_2Sb_3$ which undergoes a magnetic transition at this temperature (see section 4.4). As the magnetic structure of this minority phase is not known, these peaks were excluded from the refinement of the data with $T < 35$ K.

Magnetic symmetry analysis using BASIREPS gives for the magnetic propagation vector $\tau = [\delta\ \delta\ ½]$, for the Wyckoff position 2*c* in *P*4/*nmm*, four complex irreducible representations. Table 3 lists the real and imaginary parts of the basis vectors; $\alpha = \cos(2\pi\delta)$, $\beta = \sin(2\pi\delta)$. All four IR's were tested for fitting the high resolution data taken on D1A but none was able to refine the data satisfactorily. Only by combining BV1 of IR1 with BV2 of IR4 the intensity of the magnetic reflections were correctly fitted. The magnetic structure defined by the two BV's corresponds either to a sine-wave along the (110) direction with moments pointing in *c*-direction or to a cycloidal spiral with moments rotating within the (110) plane. In both cases the *c*-component of the magnetic propagation vector just adds an additional antiferromagnetic coupling along the *c*-axis without changing the overall aspect of the sine-wave or cycloidal spiral structure. Normally, it is not possible to differentiate from powder data between these two solutions, however, physical arguments speak in favor of

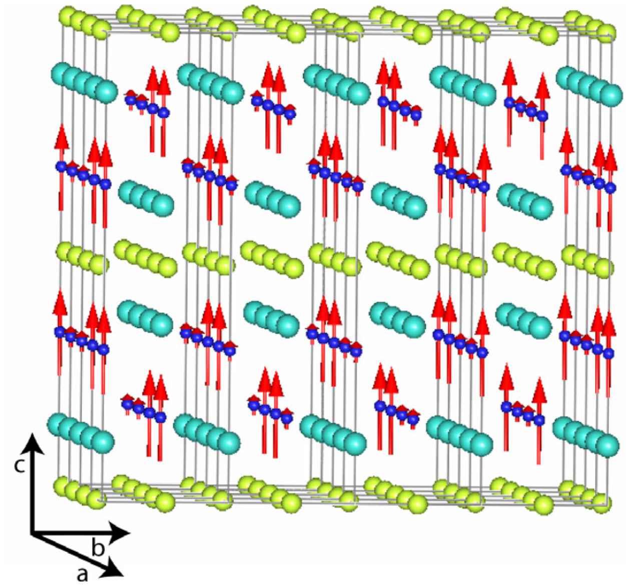

Figure 3. Magnetic structure of NdScSb at 2 K showing the superposition of $\tau_1 = [0\ 0\ 0]$ and $\tau_2 = [¼\ ¼\ 0]$; small yellow (large blue) balls represent the Sc (Sb) atoms. The slight shift of the Sc atoms from the 4*c* to the 8*j* Wyckoff position has not been taken into account.

the cycloidal spiral structure. In fact when trying to refine the data measured at the lowest temperature using the sine-wave model the maximum value of the amplitude of the magnetic moment amounts to $10.6\mu_B$ which is too large compared to the free ion value of $9\mu_B$ for Tb^{3+}.

A further argument in favor of the cycloidal model stems from the fact that when obliging the coefficients of the two BV's to produce an equal moment within the cycloidal spiral the refinement does not worsen. In table 4 the refined values of the resulting total magnetic moment and of the magnetic propagation vector are shown for different temperatures. Figure 5(*a*) shows the refinement of the data taken at $T = 62$ K; figure 5(*b*) is a picture of the magnetic structure for $\delta = 0.21$.

Looking at the refined values of the magnetic moment one can see that the values increase steadily, there is no drop between T = 40 K and 2 K. This confirms the interpretation of the additional magnetic peaks appearing at 35 K being caused by an impurity phase, as a change in the magnetic structure of the main phase at this temperature would have led to a decrease of the determined magnetic moment within the incomplete magnetic structure model.

3.2.3. PrScSb. Figure 6 shows the high intensity neutron diffraction data of PrScSb taken at 1.5 K and 20 K and the resulting difference pattern which contains the additional magnetic scattering appearing below 20 K. The magnetic transition temperature is situated below 20 K as the data taken at 30 K are similar to the 20 K data. The position of the new magnetic Bragg peaks is found at 2θ values where the extinction due to the I-centering forbids nuclear Bragg peaks. The magnetic propagation vector was determined using K-Search to be $\tau = [1\ 0\ 0]$ and the allowed IR's calculated from magnetic symmetry analysis; they are identical to those for $\tau = [0\ 0\ 0]$ displayed in table 2.

Testing the different IR's by refining the high resolution data taken on D1A it was found that the magnetic structure follows IR7 and that the magnetic moment amounts to $\mu_{Pr} = 2.54\mu_B$ at 2 K and points in the *c*-direction. Figure 7(*a*) displays the resulting fit, while figure 7(*b*) shows the magnetic structure.

3.2.4. CeScSb. Due to the low value of the magnetic moment, the magnetic scattering in CeScSb can only be made visible by creating a difference pattern between the high intensity neutron diffraction data collected each for 2 h at 2 K and 20 K. There are no new Bragg peaks arising at low temperature, the magnetic scattering appears at the position of the allowed nuclear Bragg peaks indicating a magnetic propagation vector $\tau = [0\ 0\ 0]$. In order to refine the purely magnetic scattering of the difference pattern a scale factor was determined from the refinement of the purely nuclear scattering using the 20 K data set. This scale factor is then kept fixed for the fit of the magnetic peaks. Testing the different allowed IR's (table 2) it was found that CeScSb adopts a purely ferromagnetic structure with the moments lying within the tetragonal basal plane. The direction of the magnetic moments within the *a*-*b* plane cannot be determined from powder data. The magnetic moment of $\mu_{Ce} = 0.96(4)\mu_B$ is strongly reduced compared to the expected value for a Ce^{3+} ion ($2.14\mu_B$). Figure 8(*a*) shows the refinement of the difference pattern, and figure 8(*b*) the magnetic structure. Using the high intensity D20 data, from the temperature dependence of the most intense magnetic peaks the magnetic transition temperature of $T_C \approx 9$ K was deduced.

3.3. Comparison of the magnetic structures

Figures 9(*a*) and (*b*) show the four closest $R - R$ distances existing in the CeScSi- and the CeFeSi-type compounds, respectively. Denoting the magnetic exchange interactions accordingly as J1–J4 it is possible to compare the magnetic structures of the RScSb compounds. Within the R-slabs the exchange paths J1, J2 and J4 are identical for the two structure types, however, the exchange path J3 coupling neighboring R-slabs in *c*-direction are different due to an additional shift by (½ ½ 0) in the CeFeSi-type structure. Table 5 summarizes the type of magnetic coupling found along the different pathways together with the corresponding distances.

It is seen that the predominant interaction in these RScSb compounds is of ferromagnetic nature: in CeScSb and NdScSb ($T > 22$ K) J1–J4 are exclusively ferromagnetic, while in PrScSb only J1 is antiferromagnetic. Below T = 22 K the magnetic structure of NdScSb is modulated by the second propagation vector $\tau = [¼\ ¼\ 0]$ which adds an antiferromagnetic coupling to two out of four neighbors along J1, J2 and J4, while the two other neighbors remain ferromagnetically coupled. Along J3, NdScSb has as well below T = 22 K a purely ferromagnetic coupling of the R-slabs. The situation changes for TbScSb which is the only member of the RScSb compounds studied here that adopts the CeFeSi-type structure. In contrast to the CeScSi-type compounds, the ferromagnetic coupling J3 is absent along the *c*-direction in TbScSb; instead the spin of two neighbors turns by 90° while there is

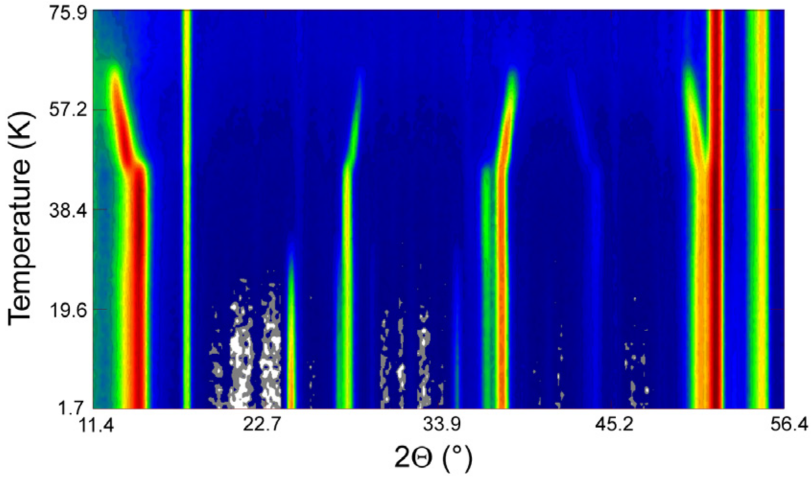

Figure 4. Thermodiffractogram of TbScSb in a 2D projection showing the magnetic phase transition at about 66 K and the variation of δ of the magnetic propagation vector $\tau = [\delta\ \delta\ ½]$ between 66 K and 40 K.

Table 3. Basis-vectors (BV) of the allowed irreducible representations (IR) for $\tau = [\delta\ \delta\ ½]$ for the Wyckoff position 2*c* of space group *P*4/*nmm*.

$\tau = [\delta\ \delta\ ½]$	BV1	BV2		BV1	BV2
IR1			IR3		
x, y, z	1 1 0 0 0 0	0 0 1 0 0 0	x, y, z	1 −1 0 0 0 0	
$-x, y, -z$	$\alpha\ \alpha\ 0$ $-\beta\ -\beta\ 0$	$0\ 0\ -\alpha$ $0\ 0\ \beta$	$-x, y, -z$	$\alpha\ -\alpha\ 0$ $-\beta\ \beta\ 0$	
IR2			IR4		
x, y, z	1 −1 0 0 0 0		x, y, z	1 1 0 0 0 0	0 0 1 0 0 0
$-x, y, -z$	$-\alpha\ \alpha\ 0$ $\beta\ -\beta\ 0$		$-x, y, -z$	$-\alpha\ -\alpha\ 0$ $\beta\ \beta\ 0$	$0\ 0\ \alpha$ $0\ 0\ -\beta$

an antiferromagnetic coupling with the other two neighbors. Together with the coupling J1 which is either 90° (two neighbors) or ferromagnetic (the other two neighbors), this leads to an antiferromagnetic alignment of the Tb-spins along the *c*-direction coupled through J3 + J1.

Comparing the above results for the RScSb compounds to similar ternary compounds adopting the CeScSi-type structure, one finds that the main interactions are again ferromagnetic: for TbZrSb, DyZrSb, NdScGe and TbScGe [8, 13], J1–J4 interactions are all ferromagnetic. For HoZrSb [13] and PrScGe [9], J1, J2 and J4 couplings are ferromagnetic, while J3 is partly (HoZrSb) or completely (PrScGe) antiferromagnetic. Within the RMgSn series of compounds [11], which crystallizes in the CeScSi-type structure, J1, J2 and J4 are again ferromagnetic while J3 is antiferromagnetic. In [11] it was proposed that the shortening of the J3 pathway (5.42 Å–5.33 Å for RMgSn with *R* = Pr, Nd, Tb) could be responsible for the establishment of an antiferromagnetic coupling along J3. This is in line with the new results for the RScSb series of compounds where the distance between *R* atoms along J3 is significantly longer (5.88 Å–5.76 Å for *R* = Ce, Nd, Pr) and the interaction is ferromagnetic. For TbScSb, crystallizing in the CeFeSi-type structure, the interaction pathway J3 is composed of the distance between neighboring R-slabs in *c*-direction plus the translational shift by ½ *a* + ½ *b* and therefore it is longer than the corresponding J3 pathway in the CeScSi-type compounds. The very short (5.50 Å) sole geometrical separation between the neighboring R-layers in *c*-direction in TbScSb could be the reason for the antiferromagnetic coupling between the slabs. It is not possible to compare TbScSb with other isostructural ternary compounds as at the moment it is the only ternary compound R-T-X with CeFeSi-type structure for which the magnetic structure is known.

Table 4. Refined values of the magnetic moment of Tb^{3+} and of the propagation vector $\tau = [\delta\ \delta\ ½]$ at different temperatures.

T[K]	μ_{Tb} [μ_B]	δ	R_{Mag}
62	4.0(1)	0.209(1)	6.3
52	6.0(1)	0.218(1)	6.1
40	7.3(1)	0.239(1)	4.4
2	7.7(1)	0.244(1)	4.7

3.4. Magnetization and heat capacity measurements

The neutron diffraction investigations described above were supplemented by magnetization (as a function of both temperature and applied magnetic field) and zero-field heat capacity measurements, as described below.

3.4.1. CeScSb. The inverse susceptibility χ^{-1} in CeScSb obeys a modified Curie-Weiss law: $\chi(T) = C/(T - \theta_p) + \chi_0$ and gives $\mu_{eff} = 2.6\ \mu_B$ (close to the free ion value of 2.54 μ_B), $\theta_p = 2.6$ K and $\chi_0 = 8 \times 10^{-4}$ emu mol^{-1} in the range 100–300 K (data not shown). Below 10 K there is an upturn in the magnetization and a thermomagnetic irreversibility between zero-field-cooled (ZFC) and field-cooled (FC) plots, see figure 10(*a*). The ZFC plot recorded in an applied field of 200 Oe shows a broad peak around 6.5 K while the FC plots increases monotonically like in a ferromagnet down to the lowest temperature. The peak at 6.5 K arises because the applied field is smaller than the coercive field of ≈ 800 Oe (at 1.8 K), see below. The in-field magnetization at 1.8 K shows a ferromagnetic-like response, acquiring a nearly saturated value of 0.9

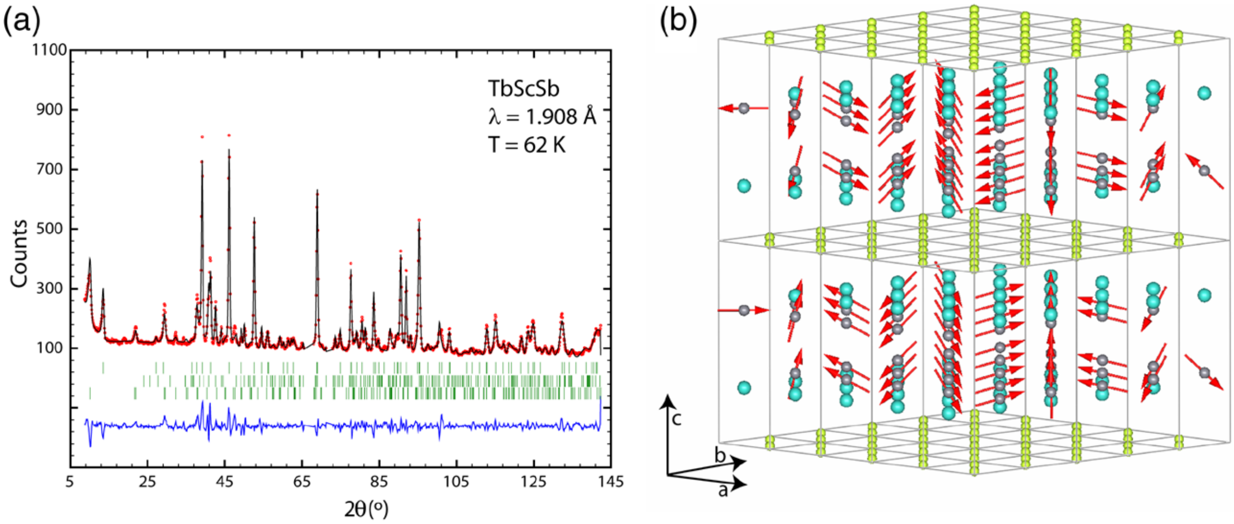

Figure 5. (*a*) Observed (dots, red), calculated (line, black) and the difference pattern of TbScSb at 62 K. The tick marks indicate the calculated position of the nuclear Bragg peaks (first row) and of the magnetic peaks (second row) of the main phase and of the $Tb_3Sc_2Sb_3$ (third row) impurity phase. (*b*) Magnetic structure of TbScSb at 62 K where τ = [0.21 0.21 ½]; small yellow (large blue) balls represent the Sc (Sb) atoms.

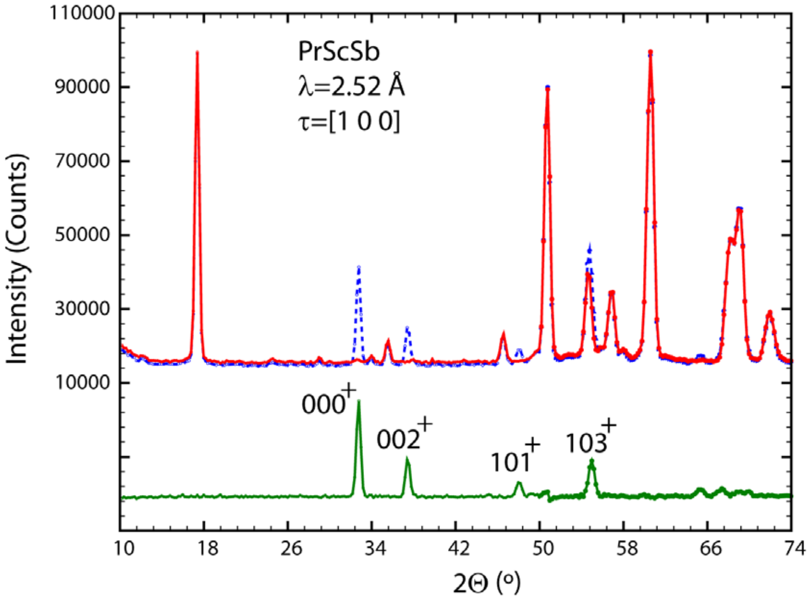

Figure 6. High intensity neutron diffraction data of PrScSb taken at 1.5 K (dotted blue line) and 20 K (solid red line) upper spectrum together with the resulting difference lower spectrum (green line) showing the purely magnetic scattering.

μ_B/f.u. at 70 kOe (see inset, figure 10(*a*)), which is comparable to 0.96(4) μ_B/f.u. inferred from neutron diffraction.

The magnetization shows hysteresis, with a coercive field of ≈ 800 Oe at 1.8 K. The magnetization data thus support the inference from neutron diffraction that a ferromagnetic transition due to the ordering of Ce moments takes place near ≈ 9–10 K. The heat capacity data shown in figure 10(*b*) lend additional confirmation of the magnetic ordering of the Ce sublattice. The heat capacity increases below ≈ 10 K attaining a value of ≈ 5.5 J mol^{-1} K at the peak temperature of ≈ 7 K, indicating a magnetic transition. The peak in the heat capacity is, however, broad, which may arise due to atomic disorder in substoichiometric $CeSc_{0.88}Sb$ (see table 1). The magnetic entropy up to 10 K, calculated after smoothly extrapolating the *C*/*T* versus *T* data to 0 K, is nearly 5 J mol^{-1} K, comparable to Rln2 (5.76 J mol^{-1} K) expected for a doublet ground state system.

3.4.2. PrScSb. The M/H data up to 80 K in PrScSb are shown in the upper inset of figure 11. A sharp peak characteristic of antiferromagnetic ordering occurs near 16 K in both the ZFC (3 kOe) and FC (50 Oe) plots. This observation is in conformity with the neutron diffraction data where an antiferromagnetic transition (figure 7(*b*)) below 20 K is inferred. The FC magnetization shows an increase at about 40 K, probably due to the presence of a small amount of impurity Pr_4Sb_3

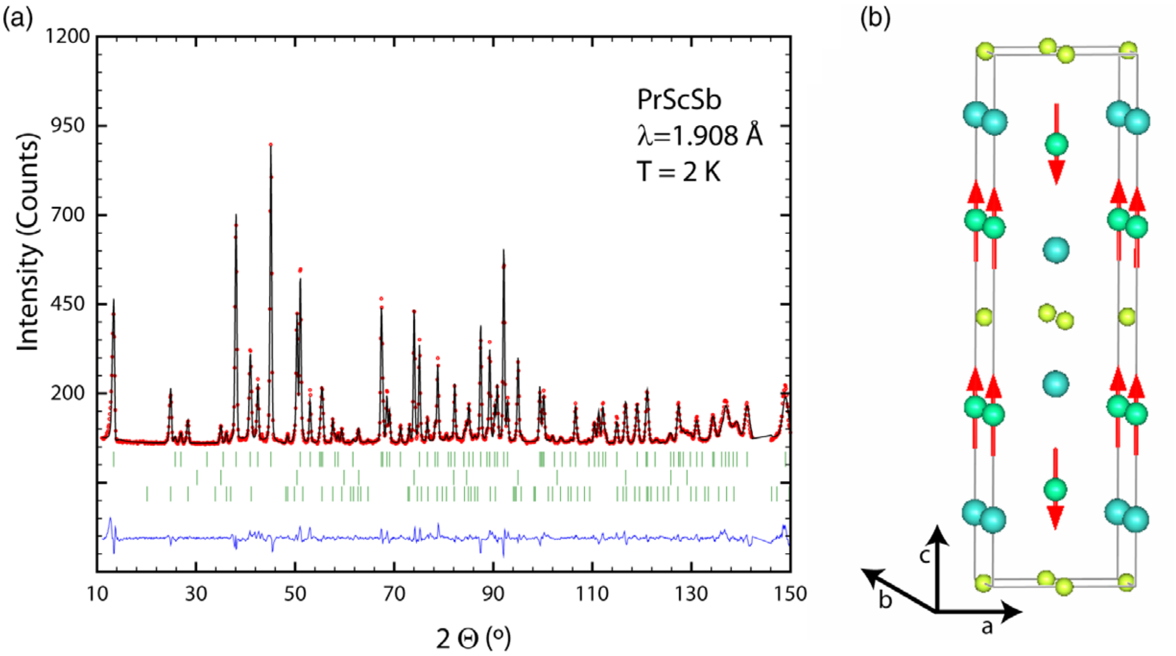

Figure 7. (*a*) Observed (dots, red), calculated (line, black) and difference pattern of PrScSb at 2 K. The tick marks indicate the calculated position of the nuclear Bragg peaks (top row) and the magnetic peaks (middle row) of the main phase and of the PrSb impurity phase (lower row). (*b*) Magnetic structure of PrScSb at 2 K with $\tau = [1\ 0\ 0]$; small yellow (large blue) balls represent the Sc (Sb) atoms.

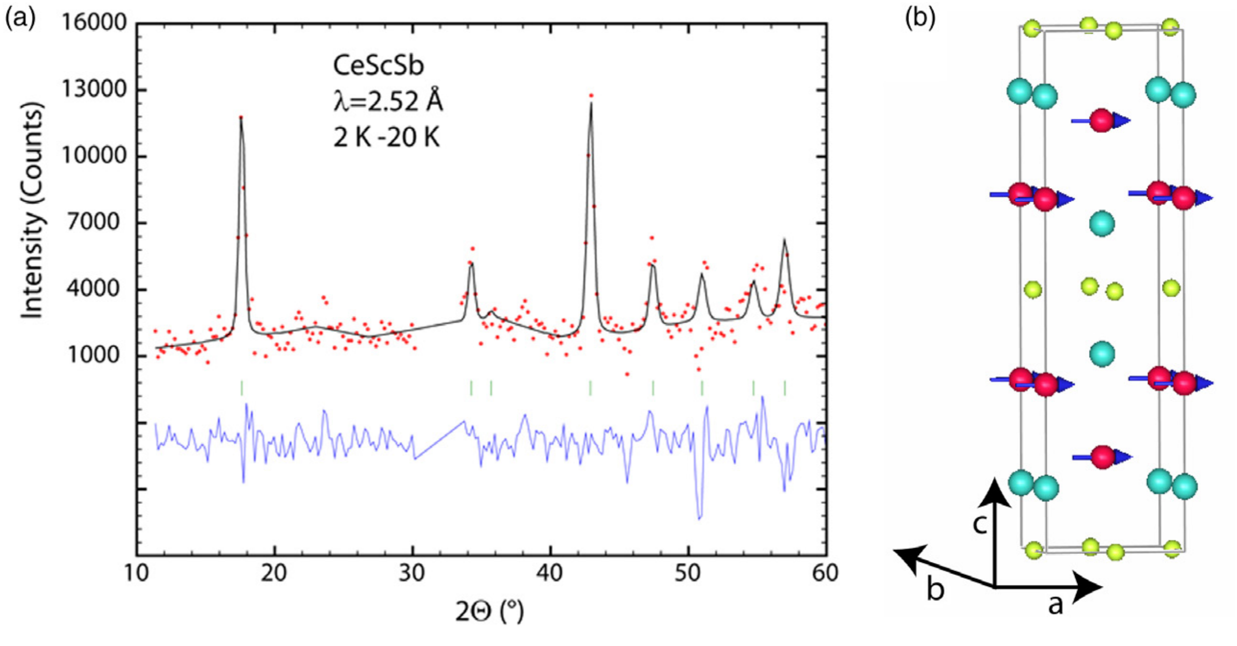

Figure 8. (*a*) Refinement of the magnetic scattering of CeScSb using a difference data set (2 K–20 K). Observed (dots, red), calculated (line, black) and difference pattern, the tick marks indicate the calculated position of the magnetic peaks. (*b*) Magnetic structure of CeScSb; small yellow (large blue) balls represent the Sc (Sb) atoms.

phase (which is known to show a spin canted AFM below 37 K [21]). Another upturn is also noticed near ≈ 28–30 K and is most likely as well due to a parasitic impurity phase.

The inverse susceptibility χ^{-1} between 1.8 and 300 K is plotted in the main panel of figure 11. Between 60 and 260 K the Curie-Weiss behavior (shown by a solid line) furnishes $\mu_{\mathrm{eff}} = 3.62\mu_{\mathrm{B}}$ and $\theta_{\mathrm{p}} = 5.8$ K. A positive θ_{p}, *prima-facie*, implies ferromagnetic exchange interactions between the Pr-ions, which is not in conformity with the AFM transition (at 16 K) of the main phase. It may be noted that in figure 7(*b*), where the AFM structure of PrScSb is shown, there are ferromagnetic layers of Pr ions in the *a*-*b* plane, aligned AFM along the *c*-axis. In such cases, a positive θ_{p} is often obtained in polycrystalline samples [22].The magnetization at 1.8 K has contributions from both AFM PrScSb and FM impurity Pr_4Sb_3.

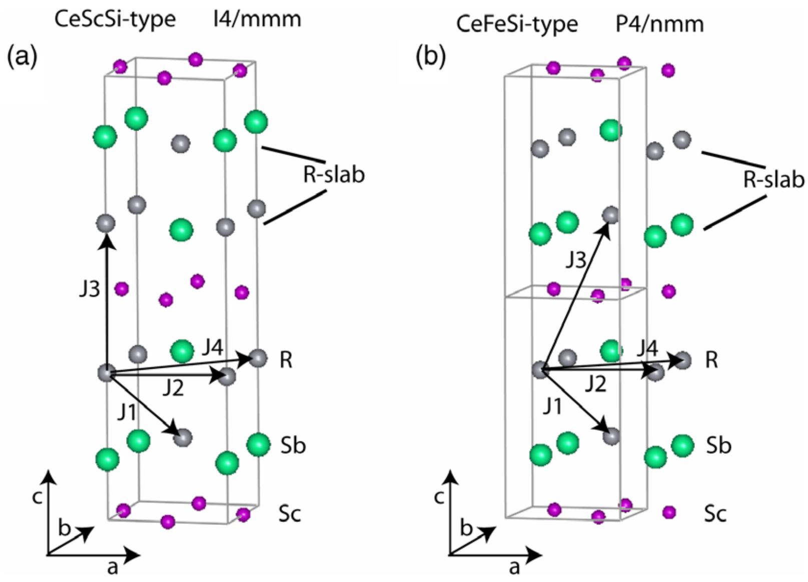

Figure 9. (*a*) CeScSi-type structure adopted by RScSb with R = Ce, Pr and Nd. (*b*) CeFeSi-type structure adopted by TbScSb. The shortest R − R distances are indicated by arrows.

Table 5. Magnetic couplings and distances J1–J4 found in the RScSb compounds (assuming $\delta = 0.25$ for TbScSb). Distances (d) are given in Å for $T = 2$ K and additionally for R = Nd as well at $T = 25$ K. F and AF correspond to ferromagnetic and antiferromagnetic coupling, respectively, while 90° means that the spin direction turns by 90° between the two neighboring sites.

	d [Å]	J1	d [Å]	J2	d [Å]	J3	d [Å]	J4
Tb, $\delta = 0.25$	4.007	F + 90°	4.306	90°	6.288	AF + 90°	6.090	AF + F
Nd, $T < 22$ K	3.943	F + AF	4.406	F + AF	5.756	F	6.230	AF + F
$T > 22$ K	3.941	F	4.406	F	5.758	F	6.230	F
Pr	3.965	AF	4.428	F	5.756	F	6.262	F
Ce	3.914	F	4.435	F	5.882	F	6.273	F

The heat capacity of PrScSb is shown in figure 12. A prominent peak in the heat capacity near 16 K confirms the bulk magnetic transition in PrScSb. The jump in the heat capacity is just ≈ 2 J mol^{-1} K and is far lower than 12.5 J mol^{-1} K, predicted by mean field theory for a spin ½ system. We believe there is substantial background heat capacity due to the presence of Schottky contribution arising from crystal electric field split levels of the Pr^{3+} ion (in addition to the phonon heat capacity), which apparently reduces the peak height at the transition. There is a hint of a minor anomaly near 30 K, which may be due to an unknown parasitic phase as speculated above in the discussion on magnetization.

3.4.3. NdScSb. The Curie-Weiss temperature dependence of the inverse susceptibility (150–300 K) furnishes a paramagnetic effective moment of 3.68μ_B and a paramagnetic Curie temperature θ_p of 5.4 K. A positive θ_p indicates ferromagnetic exchange between the Nd moments. The M/H ZFC and FC (measured at 20 Oe) and ZFC (measured at 3 kOe) plots are shown in the upper inset of figure 13. A minor jump near 72 K occurs in all the plots. Around 36–40 K the M/H plots show an upturn which continues upwards in the FC (20 Oe) plot, a behavior characteristic of FM transition. On the other hand, peaks at 32 and 20–24 K are observed in the ZFC (20 Oe and 3 kOe) plots, respectively. The plots of isothermal magnetization at 1.8, 4.5, 10, 35 and 50 K are shown in the lower inset of figure 13. The data at 50 K show an initial FM like increase at low fields and then increase linearly with the applied field at higher values. Since 50 K is well above the magnetic transition temperatures detected by the neutron diffraction, we believe the FM like increase at 50 K is due to some unidentified parasitic phase which most likely orders FM near 72 K. The M-H loops at 1.8 and 4.5 K show hysteresis, and the coercive field at 1.8 K is ≈ 18 kOe. The coercive field is surprisingly zero at 10 K, though the magnitude of the magnetization at 70 kOe at 10 K is comparable to that at 4.5 and 1.8 K. It may also be noted that the magnetization at 10, 4.5 and 1.8 K does not saturate even at 70 kOe, as would be expected in a pure ferromagnet, but it is increasing linearly. Such a behavior indicates the coexistence of FM and AFM interactions and it conforms to the results of the neutron diffraction study (table 5).

The heat capacity data are shown in figure 12. A broad shoulder develops below 36 K which is followed by a peak, albeit small, near 22 K. Below 22 K the data vary smoothly down to 1.8 K and do not show any anomaly. The peak at 22 K correlates nicely with the lower transition at the same temperature inferred from neutron diffraction. Though the appearance of a broad shoulder below 36 K correlates with the existence of a magnetic transition around 32 K seen in neutron diffraction, the lack of a sharp anomaly in the heat capacity is surprising. A broad shoulder *prima-facie* implies

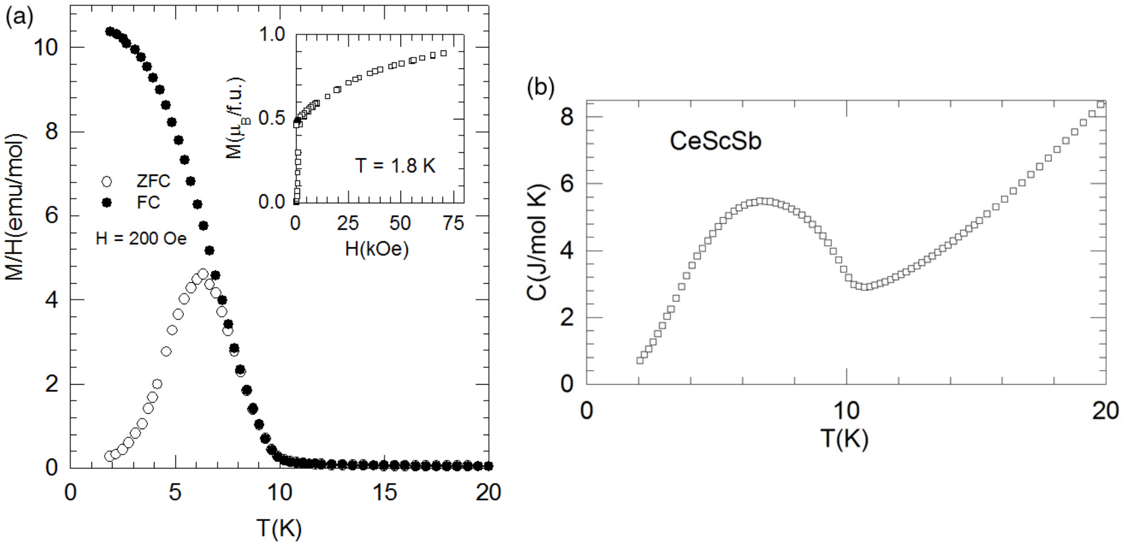

Figure 10. (*a*) The ZFC and FC magnetization of CeScSb below 20 K measured in a field of 200 Oe. The inset shows the magnetization versus field at 1.8 K up to 70 kOe. (*b*) the heat capacity of CeScSb between 1.8 and 20 K.

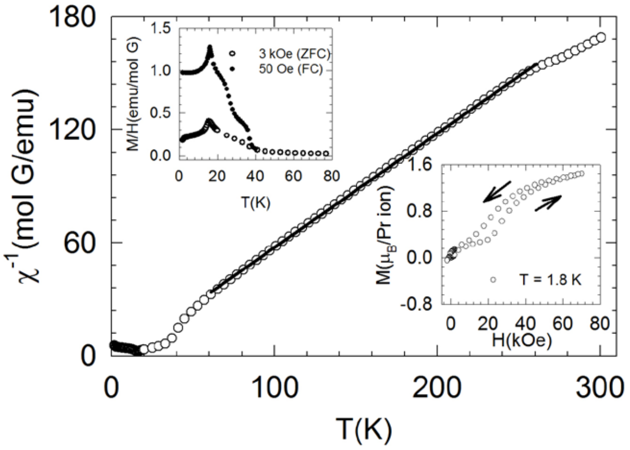

Figure 11. The inverse susceptibility of PrScSb between 1.8 and 300 K. The upper inset shows the M/H plots below 80 K taken in ZFC (3 kOe) and FC (50 Oe) mode. The lower inset shows the variation of magnetization with field at 1.8 K.

an inhomogeneous magnetic order, which is at odds with relatively sharp peak at 22 K characterizing the lower transition.

3.4.4. TbScSb. The values of the effective paramagnetic moment μ_{eff} and the paramagnetic Curie temperature θ_{p} obtained from the linear χ^{-1} versus T plot (100–300 K) are $10.3\mu_{\mathrm{B}}$ and −23 K, respectively. The μ_{eff} exceeds the free ion value ($9.72\mu_{\mathrm{B}}$) and the excess is tentatively attributed to a contribution from conduction electron polarization. Peaks in the ZFC and FC (100 Oe) plots at 69 K are in agreement with the onset of an incommensurate antiferromagnetic transition at 66 K, inferred from neutron diffraction. The ZFC and FC plots coincide with each other down to 36 K, and show a significant thermomagnetic irreversibility at lower temperatures. The latter is most likely due to the presence of a minor impurity phase of $Tb_3Sc_2Sb_3$ which in a separate investigation was found to order FM around 36 K.

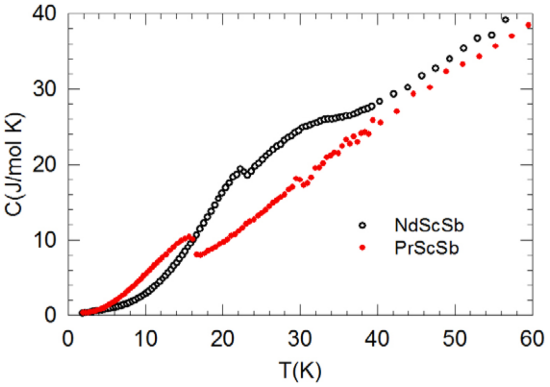

Figure 12. The heat capacity of PrScSb and NdScSb between 1.8 and 60 K.

The heat capacity data plotted in figure 14 show a prominent peak at 66.5 K confirming the bulk magnetic transition in TbScSb, which is in excellent agreement with neutron diffraction. There is no discernible peak at 36 K indicating that the amount of parasitic $Tb_3Sc_2Sb_3$ phase is indeed very small.

3.4.5. GdScSb. The χ^{-1} versus T (100–300 K) plot of GdScSb follows a Curie-Weiss behavior with $\mu_{\mathrm{eff}} = 8.2\mu_{\mathrm{B}}$ (the free ion value is $7.94\mu_{\mathrm{B}}$). The excess, like in the case of TbScSb, may be due to the contribution from conduction electron polarization. Surprisingly, θ_{p} is +33.5 K, while the sharp peak in fully overlapping ZFC and FC plots confirms an antiferromagnetic transition occurring at 56 K (see figure 15(*a*)). It was already pointed out above that a positive θ_{p} may arise in some AFM where there is FM alignment of moments within sheets and the sheets are aligned AFM. It would be interesting to find the arrangement of Gd moments in this compound. The isothermal magnetization data (figure 15(*b*)) show that the moment at 5 K in an applied field of 70 kOe is just $3\mu_{\mathrm{B}}$ per formula unit. There is a hint of a spin-flop transition at around 20 kOe but much

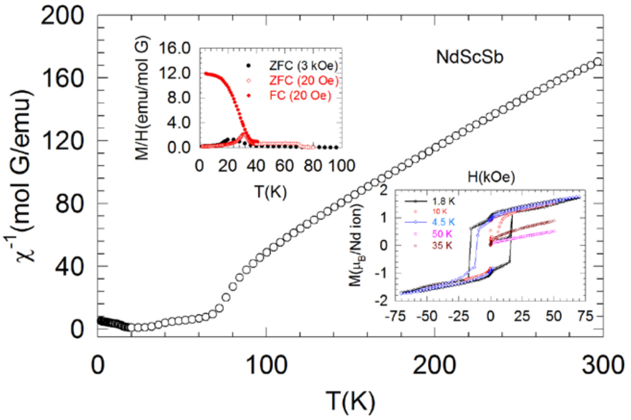

Figure 13. The inverse susceptibility of NdScSb between 1.8 and 300 K. The FC (20 Oe) and ZFC (20 Oe and 3 kOe) M/H plots between 1.8 and 100 K are shown in the upper inset. The lower inset shows the variation of magnetization with field at 1.8, 4.5, 10, 35 and 50 K.

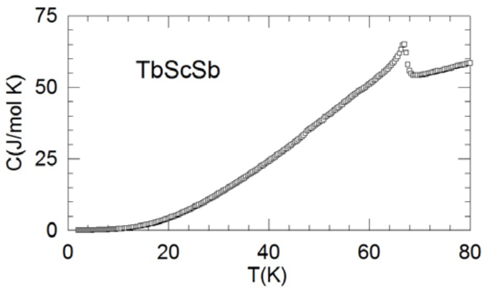

Figure 14. The heat capacity of the TbScSb compound between 1.8 and 80 K.

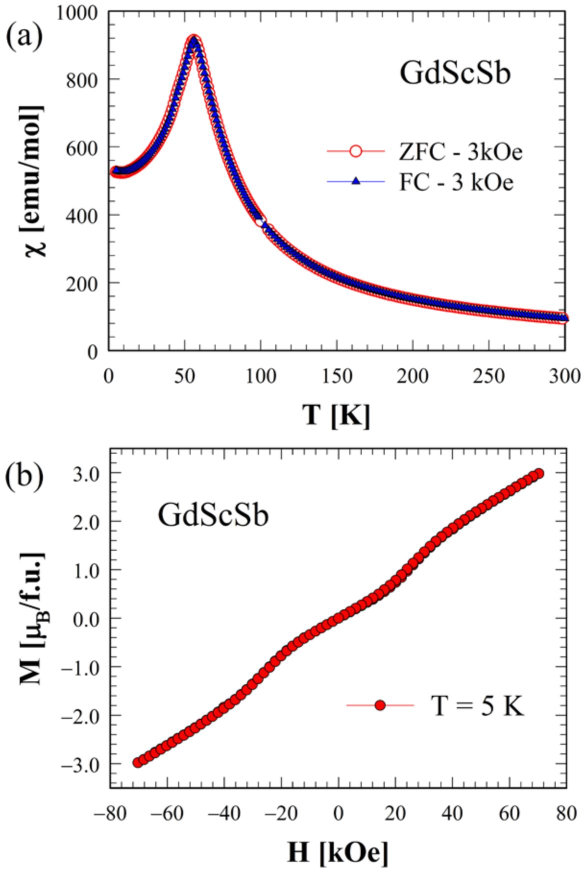

Figure 15. (*a*) ZFC and FC dc magnetization at 3 kOe for GdScSb between 2–300 K; (*b*) isothermal magnetization of GdScSb measured at 5 K up to 70 kOe.

larger fields are required for complete alignment of the moments to 7μ_B/f.u.

4. Band structure calculations

Local spin density approximation (LSDA) including Hubbard U, LSDA+U [23], calculations for GdScGe and GdScSb have been performed in conjunction with the tight-binding linear muffin tin orbital and full potential linear augmented plane wave band structure methods [24, 25]. The k-space integration has been performed with a 32 × 32 × 32 Brillouin zone mesh. This large Brillouin zone mesh was used to assure the convergence of total energy and total charge in the studied systems. For these systems, LSDA + U (with U = 6.7 eV and J = 0.7 eV) shifts the occupied 4*f* states below the Fermi level (≈ – 8.5 eV) and the unoccupied 4*f* states above the Fermi level. Since the 4*f* states are half filled in Gd compounds, the LSDA + U is considered to be the best approach for the correct positioning of occupied and unoccupied 4*f* states. In these calculations, the actual experimental structures, the CeScSi-type for GdScGe and the CeFeSi-type for GdScSb, have been used. Calculations have been done as well for GdScSb, assuming a hypothetical CeScSi-type structure, to allow a comparison with the results using the actual CeFeSi-type strucutre. The CeFeSi-type GdScSb has a lower total energy compared to the CeScSi-type GdScSb indicating the CeFeSi-type as the stable crystal structure in agreement with experiment. However, the small energy difference (≈5.6 eV cell^{-1}) between CeFeSi-type and CeScSi-type GdScSb indicates that GdScSb is indeed on the borderline of the change in structure type as the rare earth is varied. The instability of the CeScSi-type structure may be attributed to a Fermi level lying at the narrow density of states peak, while the density of states are pushed towards lower energy for the stable CeFeSi-type phase (figure 16). The antiferromagnetic total energy is lower than the ferromagnetic total energy confirming the antiferromagnetic state as the ground state in CeFeSi-type GdScSb, as opposed to the ferromagnetic state in the hypothetical CeScSi-type structure. The magnetic moment of Gd 4*f* within the ferromagnetic CeScSi-type GdScGe and hypothetical CeScSi-type GdScSb and CeFeSi-type GdScSb is identical (≈6.98μ_B). However, the Gd 5*d* moment of CeScSi-type GdScGe is 0.4μ_B, which is higher than that of the Gd 5*d* moment of CeScSi-type GdScSb (0.25μ_B) and CeFeSi-type GdScSb (0.2μ_B). This difference is due to the difference in the exchange splitting (splitting between the spin up and spin down states at the Fermi level) in these structures and systems (figure 16). Further calculations show a spin polarized Sc 3*d* moment in CeScSi-type GdScGe (0.1μ_B) and hypothetical CeScSi-type GdScSb (0.1μ_B) structures due to strong 5*d*-3*d* hybridization whereas the calculations show a negligible spin polarized Sc 3*d* moment in CeFeSi-type GdScSb. This indicates that the ferromagnetic state arising from the strong 5*d*-3*d* hybridization in

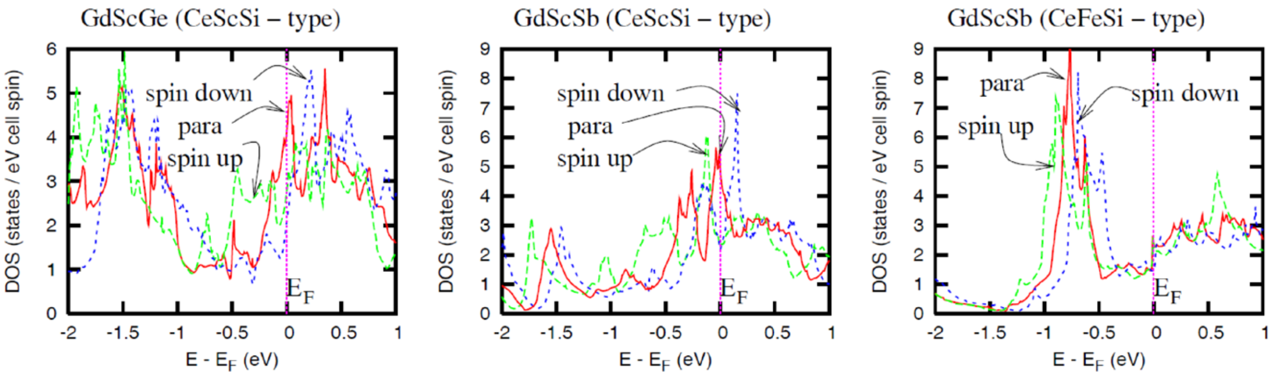

Figure 16. Spin polarized density of states of Gd in CeScSi-type GdScGe; hypothetical CeScSi-type GdScSb; and CeFeSi-type GdScSb.

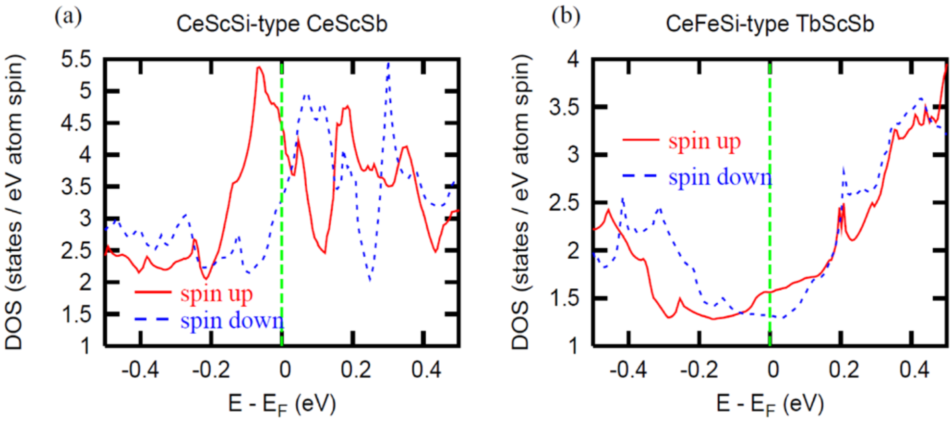

Figure 17. Spin polarized total density of states of CeScSi-type CeScSb (*a*) and CeFeSi-type TbScSb (*b*).

CeScSi-type GdScGe and hypothetical CeScSi-type GdScSb structures is missing in the CeFeSi-type GdScSb, driving this system to be antiferromagnetically stable as confirmed from total energy calculations.

The total density of states around the Fermi level of the CeScSi-type CeScSb and CeFeSi-type TbScSb compounds show substantial spin polarization and exchange splitting between spin up and spin down states across the Fermi level in CeScSi-type CeScSb (figure 17(*a*)), while spin polarization and exchange splitting are negligible in CeFeSi-type TbScSb (figure 17(*b*)). Due to the strong 5*d*-3*d* hybridization in CeScSb, Sc 3*d* exhibits 0.15μ_B magnetic moment in addition to 0.1μ_B magnetic moment of Ce 5*d*. On the other hand, TbScSb shows 0.15μ_B magnetic moment of Tb 5*d* with negligible moment in Sc atoms. The 4*f* spin moments for Ce atoms in CeScSi-type CeScSb and for Tb atoms in CeFeSi-type TbScSb are 1 and 6μ_B, as expected. Therefore, the substantial spin polarization and exchange splitting due to the 3*d*-5*d* hybridization are critical for the observed ferromagnetic behavior in CeScSi-type RScSb systems, while the absence of these characteristics support antiferromagnetism in CeFeSi-type RScSb systems.

5. Concluding summary

Within the series of ternary equiatomic RScSb compounds, the change of the structure from CeScSi-type crystallizing in space group *I4/mmm* to CeFeSi-type with space group *P4/nmm* as the rare earth atom changes from light (*R* = La-Nd, Sm) to heavy (*R* = Gd-Tm, Lu, Y) is accompanied by a change of the magnetic structure from ferromagnetic to predominantly antiferromagnetic. CeScSb and NdScSb for $T > 22$ K are simple ferromagnets, while PrScSb adopts a collinear magnetic structure where ferromagnetic sublattices of Pr-spins which are coupled through the I-centering get antiferromagnetically aligned. The presence of a second commensurate magnetic propagation vector τ = [¼ ¼ 0] leads in NdScSb below $T = 22$ K to a sin-wave like modulation of the magnetic moment values within the simple ferromagnetic configuration where, however, all spins still keep a parallel orientation. The antiferromagnetic structure found in TbScSb, determined by the incommensurate propagation vector τ = [δ δ ½], is best described as a cycloidal spiral running along the [1 1 0] direction of the tetragonal basal plane; the value of δ is temperature dependent and varies between δ = 0.21 just below T_N = 66 K and 0.244 at 2 K base temperature. Although δ never attains the commensurate value of δ = ¼ this modulation is reminiscent of the one already found at low temperatures in NdScSb with, however, the additional antiferromagnetic coupling in *c*-direction. This progressive change from ferromagnetic to antiferromagnetic interactions can tentatively be explained by the loss of the 5*d*-3*d* hybridization as the structure type changes from CeScSi (*I4/mmm*) to CeFeSi (*P4/nmm*). In fact band structure calculations show that the hybridization between the rare earth 5*d* and the scandium 3*d* bands leads to an exchange splitting between spin up and spin down bands and to substantial spin polarization across the Fermi level in the ferromagnetic CeScSi-type CeScSb which is absent in the antiferromagnetic CeFeSi-type TbScSb.

Acknowledgments

Part of this work was performed at the Ames Laboratory. The Ames Laboratory is operated by Iowa State University of Science and Technology for the U S Department of Energy; the work was supported by the Office of Basic Energy Sciences, Materials Science and Engineering Division of the Office of Science under Contract No. DE-AC02-07CH11358.

References

[1] Villars P and Calvert L D 1991 *Pearson's Handbook of Crystallographic Data for Intermetallic Compounds* 2nd edn and desk edition 1997 (Metals Park, OH: ASM)
[2] Wood G H, Rodgers J R, Villars P and Gough S R 1996 CRYSTMET: structure and powder database for metals *J. Res. Natl. Stand. Technol.* **101** 205
[3] Villars P, Prince A and Okamoto H 1995 *Handbook of Ternary Alloy Phase Diagrams* (Metals Park, OH: ASM)
[4] Legvold S 1980 Rare earth metals and alloys *Ferromagnetic Materials* ed E P Wohlfarth (Amsterdam: North-Holland) pp 183–295
[5] Singh S, Dhar S K, Manfrinetti P, Palenzona A and Mazzone D 2004 *J. Magn. Magn. Mater.* **269** 113
[6] Manfrinetti P, Pani M, Palenzona A, Dhar S K and Singh S 2002 *J. Alloys Compd.* **334** 9
[7] Tskhadadze I A, Chernyshev V V, Streletskii A N, Portnoy V K, Leonov A V, Sviridov I A, Telegina I V, Verbetskii V N, Seropegin Yu D and Morozkin A V 1999 *Mat. Res. Bull.* **34** 1773
[8] Cadogan J M, Ryan D H, Gagnon R and Voyer C J 2005 *J. Appl. Phys.* **97** 10A916
[9] Manfrinetti P, Morozkin A V, Isnard O, Henry P and Palenzona A 2008 *J. Alloys Compd.* **450** 86
[10] Vernière A, Klosek V, Welter R, Venturini G, Isnard O and Malaman B 2001 *J. Magn. Magn. Mater.* **234** 261
[11] Ritter C, Provino A, Manfrinetti P and Gschneidner K A Jr 2011 *J. Alloys Compd.* **509** 9724
[12] Lemoine P, Vernière A, Venturini G, Capelli S and Malaman B 2012 *J. Magn. Magn. Mater.* **324** 961
[13] Morozkin A V, Halich K, Welter R and Ouladdiaf B 2005 *J. Alloys Compd.* **393** 34
[14] Provino A, Paudyal D, Morozkin A V, Manfrinetti P and Gschneidner K A Jr 2014 *J. Alloys Compd.* **587** 783
[15] Rodríguez-Carvajal J 1993 *Physica* B **192** 55
[16] Chapon L C and Rodríguez-Carvajal J FullProf Studio: a program of the FullProf Suite, www.ill.eu/sites/fullprof/
[17] Wang R and Steinfink H 1967 *Inorg. Chem.* **6** 1685
[18] Abdusalyamova M N, Rahmatov O I, Faslyeva N D and Tchuiko A G 1988 *J. Less Common Met.* **141** L23
[19] Rodríguez-Carvajal J BASIREPS: a program for calculating irreducible representations of space groups and basis functions for axial and polar vector properties. Part of the FullProf Suite of programs, www.ill.eu/sites/fullprof/
[20] Ritter C 2011 *Solid State Phenom.* **170** 263
[21] Ritter C, Morozkin A V, Oskolkov K S, Nirmala R, Isnard O, Manfrinetti P and Provino A 2010 *J. Alloys Compd.* **494** 28
[22] Buschow K H J and Fast J F 1967 *Phys. Stat. Solidi* A **21** 593
[23] Anisimov V I, Aryasetiawan F and Lichtenstein A I 1997 *J. Phys.: Condens. Matter* **9** 767
[24] Andersen O K and Jepsen O 1984 *Phys. Rev. Lett.* **53** 2571
[25] Blaha P, Schwarz K, Madsen G, Kvasnicka D and Luitz J 2001 *WIEN2k*, an augmented plane wave + local orbitals program for calculating crystal properties (Austria: Karlheinz Schwarz, Techn. Universität Wien)